INTERNATIONAL JOURNAL FOR NUMERICAL METHODS IN FLUIDS
Int. J. Numer. Meth. Fluids 2016; **82**:799–817
Published online 5 May 2016 in Wiley Online Library (wileyonlinelibrary.com). DOI: 10.1002/fld.4241

Multiscale coupling of compliant and rigid walls blood flow models

Tatiana Dobroserdova[1,*,†], Maxim Olshanskii[2] and Sergey Simakov[3]

[1]*Institute of Numerical Mathematics of the Russian Academy of Sciences, Moscow, Russia; Moscow Institute of Physics and Technology (State University), Dolgoprudny, Moscow Region, Russia*
[2]*Department of Mathematics, University of Houston, Houston, Texas 77204-3008, USA*
[3]*Moscow Institute of Physics and Technology (State University), Dolgoprudny, Moscow Region, Russia; Institute of Numerical Mathematics of the Russian Academy of Sciences, Moscow, Russia*

SUMMARY

Numerical methods based on geometrical multiscale models of blood flows solve for averaged flow statistics on a network of vessels while providing more detailed information about fluid dynamics in a specific region of interest. In such an approach, a 3D model based on the Navier–Stokes equations posed in a domain with rigid walls is often used to describe blood flow dynamics in the refined region. While ignoring elasticity effects in 3D models is plausible in certain applications and saves computational time significantly, coupling such models with 1D flow models may result in non-physiological phenomena in the computed solutions. Thus, the immediate coupling conditions based on continuity of normal stresses, flow rate, pressure, or a combination of thereof do not account for the inconsistency between elasticity effects in the 1D model and the non-compliance of the 3D model. In this paper, we introduce and study an auxiliary absorbing 0D model, which is placed at the interface between 1D and 3D models. A virtual device mimics the effect of the 3D model compliance and hence reduces pressure wave reflection and instabilities caused by the inconsistency. The absorbing model is developed from basic mechanical principles. As a result, parameters of the 0D model can be designed based on hemodynamic data. We analyze the stability of the geometrical multiscale model and perform several numerical experiments to assess its computational efficiency. Copyright © 2016 John Wiley & Sons, Ltd.

Received 26 August 2015; Revised 30 March 2016; Accepted 3 April 2016

KEY WORDS: geometrical multiscale modeling; 1D-0D-3D coupling; fluid flows; cardiovascular simulations; iterative methods

1. INTRODUCTION

Geometrical multiscale modeling became nowadays a standard approach in computational hemodynamics [1–6]. Multiscale models describe blood flow in a region of interest in necessary details, while providing information about averaged flow statistics in other parts of the vascular system by employing simplified 1D flow models. The multiscale approach is particularly useful to describe complex vascular networks such as the circle of Willis [7, 8]. Because the vascular compliance is the driving mechanism of pressure wave propagation, 1D vessels are typically treated as elastic. The well-known 1D Euler equations are used to simulate the flow and pulse propagation in a vascular network. The 3D hemodynamics is described by the Navier–Stokes equations of viscous incompressible fluid. This full system of dynamic and conservation equations is often solved numerically in domains with rigid walls, because this considerably reduces the computational complexity of the problem. The major challenges of such multiscale approach are physiologically correct coupling of basic 1D and 3D models as well as the development of stable and efficient numerical algorithms.

*Correspondence to: Tatiana Dobroserdova, Institute of Numerical Mathematics of the Russian Academy of Sciences, Gubkin str., 8, Moscow, 119333, Russia.
†E-mail: DobroserdovaTK@gmail.com

A standard approach for coupling 1D and 3D fluid flow models is based on enforcing the continuity of the following quantities at the interface between 1D and 3D domains: normal stress, flow rate, total stress, pressure, vessel cross-section area, or a combination of these quantities (e.g., [1, 4, 5, 9, 10]). Applied to 1D-compliant–3D-rigid models, we call such an approach a *hard* coupling, because it does not account for the inconsistency between elastic effects in the 1D model and the non-compliance of the 3D model. The hard coupling is prone to non-physiological backward pulse-waves generated at the interface [7]. A *soft* coupling introduces an auxiliary absorbing model at the interface between 1D and 3D blood flow domains. The auxiliary model compensates for missing compliance in 3D and intends to eliminate the spurious phenomena. Thus, in [7], a 0D electric circuit model was suggested. Placed in-between blood flow models, it was found to reduce the spurious oscillations significantly and to preserve the waveform of the cardiovascular signal reasonably well over the coupling region. The success of that multiscale approach, however, requires a careful tuning of the 0D model parameters, which is done in numerical experiments.

In this report, we introduce a 0D mechanical model. The model can be interpreted as placing a (virtual) spherical balloon at the junction of two flow models. The balloon has a volume, and its wall is elastic and has a mass. This virtual device is intended to simulate the effect of missing elastic walls in the 3D model. We deduce governing equations and coupling conditions from transparent mechanical principles. This gives several advantages; in particular, the auxiliary model parameters can be derived from physiological data.

The material in the paper is organized as follows. In Section 2, we first review the 3D and 1D flow models and several coupling conditions well known from the literature. After the introduction of a 0D mechanical model in the same section, we explain how it is used for 1D-3D coupling. The cumulative energy balance of the system is studied. Further, the choice of parameters for the model is discussed. The discretization and algebraic solvers are introduced in Section 3. A second-order time-stepping algorithm with independent time steps in 3D and 1D-0D domains is used to integrate the system in time. To discretize the problem, we use a conforming inf-sup stable finite element method for the incompressible Navier–Stoke equations and a monotone finite difference scheme for 1D equations. This results in a sequence of systems of non-linear algebraic equations to be solved. We use a fixed-point method and iterate between subdomains and the coupling conditions. Finally, in Section 4, we experiment with the new multiscale model and compare soft and hard coupling conditions.

2. THE 1D-3D COUPLED MODEL

This section reviews 3D, 1D, and 0D fluid models and describes the coupling of the models.

2.1. The 3D model

We treat blood as a viscous incompressible Newtonian fluid. Assume that the fluid occupies a bounded domain $\Omega \subset \mathbb{R}^3$. We distinguish between the 'open' part of boundary and the no-slip–no-penetration part (rigid walls), Γ_0. The open boundary is conventionally divided into the inflow Γ_{in} and the outflow Γ_{out} parts. The open boundary conditions are defined by setting the normal stress tensor equal to given vector functions $\boldsymbol{\phi}$ and $\boldsymbol{\gamma}$. These open boundary conditions are studied in [11]. Thus, the 3D model consists of the classical Navier–Stokes equations in pressure–velocity variables with suitable boundary conditions:

$$\begin{cases} \rho\left(\frac{\partial \mathbf{u}}{\partial t} + (\mathbf{u}\cdot\nabla)\,\mathbf{u}\right) - \nu\Delta\mathbf{u} + \nabla p = \mathbf{0} & \\ \operatorname{div}\mathbf{u} = 0 & \text{in } \Omega, \\ \mathbf{u} = \mathbf{0} & \text{on } \Gamma_0, \\ \nu\frac{\partial \mathbf{u}}{\partial \mathbf{n}} - p\mathbf{n} = \boldsymbol{\phi} & \text{on } \Gamma_{\text{in}}, \\ \nu\frac{\partial \mathbf{u}}{\partial \mathbf{n}} - p\mathbf{n} = \boldsymbol{\gamma} & \text{on } \Gamma_{\text{out}}. \end{cases} \tag{1}$$

Here, $\mathbf{n}$ is the outward normal vector to $\partial\Omega$, $\mathbf{u}$ is the vector field of fluid velocity, p is the pressure, ν, and ρ are given fluid viscosity and density constant coefficients. The system is also supplemented with initial condition $\mathbf{u} = \mathbf{u}_0$ ($\operatorname{div}\mathbf{u}_0 = 0$) for $t = 0$ in Ω.

DOI: 10.1002/fld

We remark that the notion of 'inflow' and 'outflow' boundary is used here and further in the text conventionally, because the inequalities $\mathbf{u}\cdot\mathbf{n} < 0$ or $\mathbf{u}\cdot\mathbf{n} > 0$ are *not* necessarily pointwise satisfied on Γ_{in} or Γ_{out}, respectively.

2.2. The 1D model

A 1D model of blood flow in a vessel is analogous to the model of viscous incompressible fluid flow through a long elastic tube. It is derived from the 3D Navier–Stokes equations and mass continuity equation assuming the small ratio of the diameter and the length of the tube (e.g., [12–14]). Denote by x the coordinate along the centerline of the tube. Let $\omega(t,x)$ be the normal cross-section of the tube at x. Denote by $S(t,x)$ the area of $\omega(t,x)$ and by $u(t,\boldsymbol{x})$ the axial velocity. We introduce the mean axial velocity $\bar{u}$ and pressure averaged over cross section $\omega(t,x)$:

$$\bar{u}(t,x) = \frac{1}{S(t,x)}\int_{\omega(t,x)} u(t,\mathbf{x})\mathbf{ds}, \quad \bar{p}(t,x) = \frac{1}{S(t,x)}\int_{\omega(t,x)} p(t,\mathbf{x})\mathbf{ds}.$$

We consider the model given by the following system of equations for unknowns $S, \bar{u}, \bar{p}$:

$$\begin{cases} \frac{\partial S}{\partial t} + \dfrac{\partial(S\bar{u})}{\partial x} & = \varphi(t,x,S,\bar{u}) \\ \frac{\partial \bar{u}}{\partial t} + \dfrac{\partial\left(\bar{u}^2/2 + \bar{p}/\rho\right)}{\partial x} & = \psi(t,x,S,\bar{u}) \\ \bar{p} & = p_{\text{ext}} + \rho c_0^2 f(S) \end{cases} \qquad \text{for } x \in [0,b]. \tag{2}$$

Here, p_{ext} is the external pressure, $\varphi(t,x,S,\bar{u})$ is a function modeling the source or the sink of the fluid. Further, we assume $\varphi = 0$ and $p_{\text{ext}} = 0$, so from now $\bar{p}$ has the meaning of the difference between the fluid pressure and the external pressure. The term $\psi(t,x,S,\bar{u})$ accounts for external forces, such as gravity or friction. Following [15], we set $\psi = -16\nu\bar{u}\eta(\tilde{S})(\tilde{S}d^2)^{-1}$, $\tilde{S} = \widehat{S}^{-1}S$. Here, ν is the viscosity coefficient, d is the pipe diameter, $\widehat{S}$ is the reference area (in the hemodynamic applications $\widehat{S}$ is the cross-section area corresponding to zero transmural pressure), and $\eta(\tilde{S})$ is a strictly positive function (see [9] for the particular choice of η). The last equation in (2) relates the pressure to the cross section area. The function f is defined by the elasticity model of the pipe walls, c_0 is the propagation speed of small disturbances in the vessel's wall material. It accounts for unstressed vessels elasticity in the 1D model. We use the model from [15]:

$$f(\tilde{S}) = \begin{cases} \exp(\tilde{S}-1) - 1, & \tilde{S} > 1, \\ \ln\tilde{S}, & \tilde{S} \leqslant 1. \end{cases} \tag{3}$$

Other algebraic defining relations linking the mean pressure and the cross-section area are known from the literature (e.g., [14]). They are equally well suited for the purpose of this paper and require a minor modification of the analysis. More sophisticated 1D models posed on vessels networks can be found, for example, in [8, 16].

Initial conditions for (2) are set to be $\bar{u}|_{t=0} = u_0$, $S|_{t=0} = S_0$. System (2) is hyperbolic and can be integrated along its characteristics. Two boundary conditions, one at $x = 0$ and one at $x = b$, are enough to close the system.

2.3. The 1D-3D model: hard coupling

Assume the 1D flow model is coupled to a part of open boundary $\Gamma \subset \partial\Omega_{3\text{D}}$ of the 3D flow model (see the illustration in Figure 1).

The continuity of the normal stress on Γ is one condition commonly imposed at the interface:

$$\left(-\nu\frac{\partial\mathbf{u}}{\partial\mathbf{n}} + p\mathbf{n}\right)\Big|_{\Gamma} = \bar{p}|_{x=b}\mathbf{n}, \tag{4}$$

DOI: 10.1002/fld

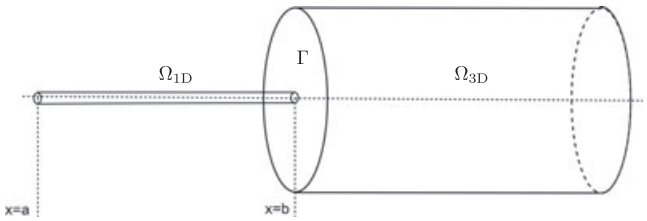

Figure 1. A simple multiscale 1D-3D model. Coupling conditions are prescribed for Γ and $x = b$.

where $\mathbf{n}$ is an outward normal vector for Ω_{3D}. Condition (4) is natural for a weak formulation of the Navier–Stokes equations written in convection or conservation forms. When prescribed on the inflow and outflow boundaries, the boundary condition (4) corresponds to so-called pressure drop problem [11].

The continuity of the flow rate is another standard condition at the interface:

$$\int_{\Gamma} \mathbf{u} \cdot \mathbf{n}\, ds = -S\bar{u}|_{x=b}. \tag{5}$$

The pair of coupling conditions (4) and (5) ensures the mass conservation for the multiscale model. At the same time, this choice is known to violate the energy balance of the system. Alternatively, (5) can be combined with the continuity condition for the normal *total* stress [10]. Also the continuity of the fluid flux and the energy flux combination can be prescribed to deal with energy inconsistency [9]:

$$\bar{p} \int_{\Gamma} \mathbf{u} \cdot \mathbf{n} \mathbf{ds} + \frac{\rho}{2} \int_{\Gamma} |\mathbf{u}|^2 (\mathbf{u} \cdot \mathbf{n}) \mathbf{ds} = -\left(\bar{p} S\bar{u} + \frac{\rho}{2} S\bar{u}^3\right)|_{x=b}, \tag{6}$$

leading to the correct energy balance and hence to the fundamental energy estimate, at the expense of global mass conservation.

The hard coupling of a 1D-elastic and the 3D-rigid models is sufficiently effective as a downstream coupling condition. However, it may produce reflected spurious pressure waves [14, 17], especially if the interface is located upstream. The spurious oscillations may spoil the numerical solution making it physiologically irrelevant. Therefore, one is prompted to look for more flexible (soft) coupling conditions.

2.4. The 1D-0D-3D model: soft coupling

First, we deduce a suitable absorbing 0D model. To this end, consider an elastic sphere Ω_{0D} of volume $V = V(t)$ filled with a fluid (blood). At any time instance $t \in [0, T]$, assume a homogeneous pressure distribution in Ω_{0D}. The variable $p_{0D} = p_{0D}(t)$ has the meaning of the difference between fluid and external pressures for the sphere, and so p_{0D} can be non-positive. The reference volume V_0 for the sphere 'at rest' is prescribed for $p_{0D} = 0$. The kinematics of the sphere under the action of fluid pressure is described by the following ODE

$$I \frac{d^2V}{dt^2} + R_0 \frac{dV}{dt} + \frac{V - V_0}{C} = p_{0D}. \tag{7}$$

Here, the expansibility factor C and the resistance coefficient R_0 characterize the elastic properties of the sphere walls. The second-order term accounts for the inertia effects. The coefficient I is positive, if one prescribes a non-zero mass to the elastic walls of the sphere; otherwise, one may set $I = 0$. In [15], Eq. 7 was considered as a part of the dynamic heart model: each of the four chambers was represented by an elastic sphere. Here, we use the hydraulic model as an auxiliary one for the coupling of vessels networks.

DOI: 10.1002/fld

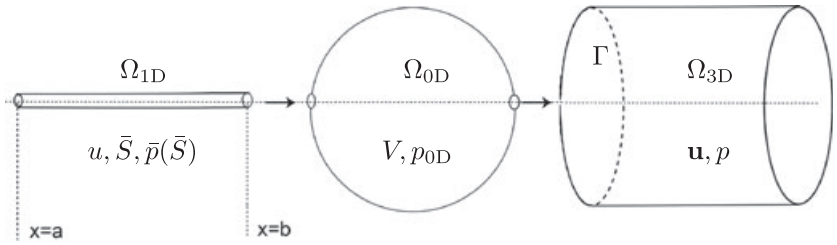

Figure 2. The schematic coupling of Ω_{1D}, Ω_{0D}, and Ω_{3D} domains.

Similar to [7], we place the 0D model at the interface of 1D and 3D models. The virtual absorbing device modeled by (7) is supposed to mimic the effect of the 3D model compliance and so to reduce pressure wave reflection and instabilities caused by the inconsistency of elastic-rigid coupling.

Now, we couple the hydraulic model to 1D and 3D blood flow models. Because we treat the blood as an incompressible fluid, the conservation of mass leads to the following equation for the rate of volume change:

$$\frac{dV}{dt} = Q_{1D} - Q_{3D}, \tag{8}$$

where $Q_{1D} = S\bar{u}$ is the fluid flux at $x = b$ and $Q_{3D} = -\int_\Gamma \mathbf{u}\cdot\mathbf{n}\, ds$ is the fluid flux through Γ (from Ω_{0D} to Ω_{3D}). Finally, we assume the Poiseuille law, which links the flow rate to the pressure drop:

$$\bar{p} - p_{0D} = R_{1D0D} Q_{1D} \quad \text{at } x = b, \tag{9}$$

$$p_{0D} - p = R_{0D3D} Q_{3D} \quad \text{on } \Gamma, \tag{10}$$

where R_{1D0D} and R_{0D3D} are the resistance coefficients. Thus, Eqs. 7–(10) form the complete set of coupling and absorbing conditions. Figure 2 illustrates the new geometrical multiscale model.

Remark 2.1
For $R_{1D0D} = R_{0D3D} = I = R_0 = 0$ and $C \to 0$, the relations (7)–(10) reduce to the hard 1D-3D coupling based on the flow rate (5) and the continuity of pressure $p = \bar{p}$. For the particular case of $I = R_0 = 0$, the model is formally equivalent (up to prescribing particular values to other coefficient) to the electric circuit model with zero inductance from [7]. More important is that the clear mechanical interpretation of the present multiscale model leads to the choice of parameters based on physical properties of modeled fluids and materials. We also note from (7)–(10) that 1D and 3D quantities do not depend on the prescribed value of V_0. Actually, the substitution $V \to V + V_0$ eliminates V_0 from the system and one can consider V as the difference of initial and current volumes of the sphere.

Remark 2.2
In practice, one may be interested in embedding the 3D domain in a 1D network of blood vessels. In such a situation, coupling between 3D and 1D domains happens on both upstream and downstream parts of the 3D domain. The downstream part of the 1D network may influence the upstream coupling by generating additional resistance to the impulse propagation. The studies in [7] show that it can be necessary to introduce the 0D model also on the downstream interface. In the present paper, we concentrate on upstream coupling, but also experiment with a 1D-0D-3D-1D configuration, where 1D represents a single vessel. We plan to study the embedding of the 3D domain in a 1D network in the future.

2.5. Energy balance

It is well known that the energy balance of the system depends on the interface conditions [1]. There was a significant interest recently in the design of 1D-3D models coupling conditions such that the

DOI: 10.1002/fld

whole system dissipates energy in the absence of external sources (e.g., [9, 10]). Below we study how introducing of the 0D auxiliary model alters the energy balance of the system.

For the sufficiently smooth solution of the Navier–Stokes system (1), the following energy balance holds:

$$\frac{d}{dt}\mathcal{E}_{3D}(t) + \nu\|\nabla\mathbf{u}\|^2 + \int_{\Gamma_{\text{in}}}\left(\frac{\rho}{2}|\mathbf{u}|^2\mathbf{n} - \boldsymbol{\phi}\right)\cdot\mathbf{uds} + \int_{\Gamma_{\text{out}}}\left(\frac{\rho}{2}|\mathbf{u}|^2\mathbf{n} - \boldsymbol{\gamma}\right)\cdot\mathbf{uds} = 0,$$

with kinetic energy $\mathcal{E}_{3D}(t) = \frac{\rho}{2}\|\mathbf{u}\|^2$. Here and in the rest of the paper, $\|\cdot\|$ denotes the $L^2(\Omega)$ norm. Because the 3D model is rigid the kinetic energy equals the total energy here.

The 1D model (2) leads to the following energy equality (we assume $\varphi = 0$):

$$\frac{\mathrm{d}}{\mathrm{dt}}\mathcal{E}_{1D}(t) - \rho\int_0^b S\psi(t,x,S,\bar{u})\,\bar{u}\mathrm{dt} = -S\bar{u}\left(\bar{p} + \frac{\rho}{2}\bar{u}^2\right)\Big|_0^b, \tag{11}$$

with the energy functional

$$\mathcal{E}_{1D}(t) = \frac{\rho}{2}\int_0^b S\bar{u}^2\mathrm{dx} + \int_0^b\int_{\widehat{S}}^S f(s)\mathrm{d}s\mathrm{dx}.$$

For $f(S)$ given in (3), the second term in the definition of $\mathcal{E}_{1D}(t)$ corresponds to the free energy of the elastic walls and is always positive, making $\mathcal{E}_{1D}(t)$ positive for all $t > 0$. The choice of $\psi(t,x,S,\bar{u})$ ensures that the second term on the left-hand side of (11) is positive as well.

For the potential and kinetic energy of the linear harmonic oscillator described by Eq. 7, we have

$$\mathcal{E}_{pot,0D}(t) = \frac{(V-V_0)^2}{2C}, \quad \mathcal{E}_{kin,0D}(t) = \frac{I}{2}\left(\frac{dV}{dt}\right)^2.$$

Using (7)–(8), we compute for the rate of change of the total energy of the elastic sphere:

$$\begin{aligned}\frac{d}{dt}\mathcal{E}_{0D}(t) &= \frac{dV}{dt}\frac{(V-V_0)}{C} + I\frac{dV}{dt}\frac{d^2V}{dt^2} = \frac{dV}{dt}\left(p_{0\text{D}} - I\frac{d^2V}{dt^2} - R_0\frac{dV}{dt}\right) + I\frac{dV}{dt}\frac{d^2V}{dt^2}\\ &= \frac{dV}{dt}\left(p_{0\text{D}} - R_0\frac{dV}{dt}\right) = (Q_{1\text{D}} - Q_{3\text{D}})p_{0\text{D}} - R_0(Q_{1\text{D}} - Q_{3\text{D}})^2.\end{aligned}$$

From (9)–(10), we compute $p_{0\text{D}} = \frac{1}{2}(\bar{p} + p + R_{0\text{D}3\text{D}}Q_{3\text{D}} - R_{0\text{D}1\text{D}}Q_{1\text{D}})$. Substituting these equalities into the previous expression, we get after straightforward calculations

$$\begin{aligned}\frac{d}{dt}\mathcal{E}_{0D}(t) = &-\frac{1}{4}\left(R_{0\text{D}3\text{D}} + R_{0\text{D}1\text{D}} + 4R_0\right)(Q_{1\text{D}} - Q_{3\text{D}})^2 - \frac{1}{4}\left(R_{0\text{D}1\text{D}} - R_{0\text{D}3\text{D}}\right)(Q_{1\text{D}}^2 - Q_{3\text{D}}^2)\\ &+ \frac{1}{2}\left(\bar{p} + p\right)(Q_{1\text{D}} - Q_{3\text{D}}).\end{aligned}$$

To see more explicitly how the coupling conditions enter the energy balance, let us assume no inflow or outflow through the open end of 1D model and the open boundary of the 3D model. For further cancelations, set the resistance coefficients equal: $R_{\text{total}} = 2R_{0\text{D}1\text{D}} = 2R_{0\text{D}3\text{D}}$. Using the definition of fluxes, we get

$$\begin{aligned}&\frac{d}{dt}\left(\mathcal{E}_{3D}(t) + \mathcal{E}_{1D}(t) + \mathcal{E}_{0D}(t)\right)\\ &= -\nu\|\nabla\mathbf{u}\|^2 + \rho\int_0^b S\psi(t,x,S,\bar{u})\,\bar{u}\mathrm{dt} - \frac{1}{4}(R_{\text{total}} + 4R_0)(Q_{1\text{D}} - Q_{3\text{D}})^2\\ &\quad - \int_\Gamma\left(\frac{\rho}{2}|\mathbf{u}|^2\mathbf{n} - \nu\frac{\partial\mathbf{u}}{\partial\mathbf{n}} + p\mathbf{n}\right)\cdot\mathbf{uds} - Q_{1\text{D}}\left(\bar{p} + \frac{\rho}{2}\bar{u}^2\right) + \frac{1}{2}\left(\bar{p} + p\right)(Q_{1\text{D}} - Q_{3\text{D}})\end{aligned}$$

DOI: 10.1002/fld

$$= -\nu\|\nabla\mathbf{u}\|^2 + \rho\int_0^b S\psi(t,x,S,\bar{u})\,\bar{u}\mathrm{d}t - \frac{1}{4}(R_{\text{total}} + 4R_0)(Q_{1\text{D}} - Q_{3\text{D}})^2$$
$$- \int_\Gamma \frac{\rho}{2}|\mathbf{u}|^2(\mathbf{n}\cdot\mathbf{u})\mathbf{ds} - Q_{1\text{D}}\frac{\rho}{2}\bar{u}^2 - \frac{1}{2}(\bar{p} - p)(Q_{1\text{D}} + Q_{3\text{D}}).$$

From (9)–(10), we get $\bar{p} - p = R_{0\text{D}3\text{D}}Q_{3\text{D}} + R_{0\text{D}1\text{D}}Q_{1\text{D}} = \frac{1}{2}R_{\text{total}}(Q_{3\text{D}} + Q_{1\text{D}})$. Substituting into the previous expression, we obtain the following balance for the cumulative energy of the system:

$$\begin{aligned}
&\frac{d}{dt}\left(\mathcal{E}_{3D}(t) + \mathcal{E}_{1D}(t) + \mathcal{E}_{0D}(t)\right)\\
&= -\nu\|\nabla\mathbf{u}\|^2 + \rho\int_0^b S\psi(t,x,S,\bar{u})\,\bar{u}\mathrm{d}t - \frac{1}{4}(R_{\text{total}} + 4R_0)(Q_{1\text{D}} - Q_{3\text{D}})^2\\
&\quad - \frac{1}{4}R_{\text{total}}(Q_{1\text{D}} + Q_{3\text{D}})^2 - \int_\Gamma \frac{\rho}{2}|\mathbf{u}|^2(\mathbf{n}\cdot\mathbf{u})\mathbf{ds} - Q_{1\text{D}}\frac{\rho}{2}\bar{u}^2
\end{aligned} \tag{12}$$

Energy balance for the hard coupling follows from (12) if one sets $R_{\text{total}} = R_0 = 0$. We note that the multiscale coupling introduces additional dissipation both through positive R_0 and positive R_{total}.

2.6. The choice of parameters

Assume that the 0D model is introduced to mimic the compliance of a vessel segment of the reference length l; and the elasticity properties of the vessel can be approximated by the constitutive Eq. 3. Following [18], the choice of resistance coefficients $R_{1\text{D}0\text{D}}$ and $R_{0\text{D}3\text{D}}$ can be done based on the characteristic impedance of the 1D model

$$R_{1\text{D}0\text{D}} + R_{0\text{D}3\text{D}} = \frac{\rho c_0}{\widehat{S}}. \tag{13}$$

Performing experiments, we found that the distribution of the resistance between $R_{1\text{D}0\text{D}}$ and $R_{0\text{D}3\text{D}}$ does not influence the results in any significant way. The total resistance appears to be important.

Now we discuss how to choose another important parameter: the virtual elastic sphere expansibility factor C. First, from Eq. 7 for $I = R_0 = 0$, we get

$$\frac{1}{C} = \frac{\Delta p_{0\text{D}}}{\Delta V}$$

Because the 0D model should account for the missing vessel compliance, the change in the volume of the sphere can be assumed equal to the change of (averaged) cross-section times the reference length of the rigid domain, $\Delta V = \Delta(lS)$. For the change of 0D pressure, we assume the same constitutive Eq. 3 to be valid. Hence, we get

$$\frac{1}{C} = \frac{\Delta(\rho c_0^2 f(S))}{\Delta(lS)} = \frac{\rho c_0^2}{l}\frac{\partial f(S)}{\partial S}.$$

One computes

$$\frac{\partial f(S)}{\partial S} = \begin{cases} \widehat{S}^{-1}\exp\left(S\widehat{S}^{-1} - 1\right), & \text{for } S > \widehat{S}\\ S^{-1}, & \text{for } S \leqslant \widehat{S}. \end{cases}$$

Assuming *small* deformations, it holds

$$\frac{\partial f(S)}{\partial S} \sim \widehat{S}^{-1}.$$

Thus, for the case of small deformations, we arrive at the expression for the expansibility factor

$$C = \frac{l\widehat{S}}{\rho c_0^2}. \tag{14}$$

DOI: 10.1002/fld

In numerical experiments, we observed that coefficient C and the value of total resistance $R_{1D0D} + R_{0D3D}$ are important for a suitable performance of the coupled system. We experimented with several values of $R_0 > 0$, but did not see a notable difference in results, at least with coefficients R_{1D0D}, R_{0D3D} and C chosen based on the aforementioned formulae. Numerical results presented in Section 4 were computed with $R_0 = 0$. We are considering zero inertia ($I = 0$) of the 0D model walls. This parameter choice makes the coupling conditions formally equivalent to those from [7]. It is the choice of other parameters (and numerical method) that differs from the present approach. It is possible that applied to different hemodynamic problems, other than that studied in Section 4, one would benefit from another (non-zero) choice of R_0 and I. We shall look for and study such problems elsewhere.

3. DISCRETIZATION AND ALGEBRAIC SOLVER

In this section, we explain our time-stepping algorithm and an iterative domain decomposition method.

For the hyperbolic equations in 1D domain, the time step is constrained by the Courant condition, and in our application, Δt_{1D} turns out to be close to 10^{-5}. Using the same time step for computing the 3D model is prohibitory expensive. Hence, we use different Δt_{1D} and Δt_{3D} for 1D and 3D parts of multiscale model, respectively. Typically, it holds $\Delta t_{1D} \ll \Delta t_{3D}$. We note that using an unconditionally stable implicit scheme is possible for 1D equations. However, this leads to large coupled systems in the case of 1D graph of vessels. Thus, we consider it important to couple 3D solver with 1D explicit method.

We associate the nth time step in 1D with the Nth time step in 3D if it holds $(n-1)\Delta t_{1D} < N\Delta t_{3D} \leqslant n\Delta t_{1D}$. Assume that the numerical solution is known for $T_k = k\Delta t_{3D}$, $k = 1, ..., N$ in Ω_{3D} and Ω_{0D}, and for $t_k = k\Delta t_{1D}$, $k = 1, ..., n$ in Ω_{1D}. We compute numerical solutions of the coupled model at T_{N+1} in Ω_{3D} and Ω_{0D} and for t_k, $k = n+1, ..., n+m$ in Ω_{1D} (m is such that $(n+m-1)\Delta t_{1D} < (N+1)\Delta t_{3D} \leqslant (n+m)\Delta t_{1D}$). This is done with the help of the iterative domain decomposition algorithm below.

3.1. Iterative domain-decomposition method

Index i will refer to inner iterations. The inner tolerance is $\varepsilon > 0$, the maximum number of iterations is denoted by N_{iter}, and $\chi \in (0, 1]$, $\omega \in (0, 1]$ are the relaxation parameters. We shall use the notation $p^i_{3D} \in \mathbb{R}$ for the ith iterate to the value prescribed on Γ as a boundary condition for the 3D problem.

We initialize $Q^0_{3D}(T_{N+1}) = Q_{3D}(T_N)$, $V^0(T_{N+1}) = V(T_N)$, $Q^1_{1D}(T_{N+1}) = Q_{3D}(T_N)$ and iterate for $i = 0, 1, 2, \ldots$, while $|p^{i+1}_{3D}(T_{N+1}) - p^i_{3D}(T_{N+1})| > \epsilon$ and $i < N_{\text{iter}}$:

Step 1. Using (8), calculate the fluid flux at the downstream end of the interval Ω_{1D}:

$$Q^{i+1}_{1D}(T_{N+1}) = (1-\omega)Q^i_{1D}(T_{N+1}) + \omega\left[Q^i_{3D}(T_{N+1}) + \left(\frac{dV}{dt}\right)^i(T_{N+1})\right].$$

Step 2. Integrate 1D problem (2) for $t \in [T_N, T_{N+1}]$, with a given fluid flux or velocity as an upstream condition at $x = a$ and the downstream condition given by

$$Q_{1D}(t_k)^{i+1} = h(Q_{1D}(T_N), Q^{i+1}_{1D}(T_{N+1}), t_k), \;\; k = n+1, ..., n+m, \;\; \text{at } x = b,$$

where $h(b(t_1), b(t_2), t_3)$ interpolates values $b(t_1)$, $b(t_2)$ at time t_3. Hence we also obtain $\bar{p}^{i+1}(T_{N+1})|_{x=b}$.

Step 3. Because we assume the inertia coefficient I equals zero, Equations (7), (8), and (9) lead to

$$V^{i+1}(T_{N+1}) = V_0 + C\left(\bar{p}^i(T_{N+1})|_{x=b} - (R_{1D0D} + R_0)Q^{i+1}_{1D}(T_{N+1}) + R_0 Q^i_{3D}(T_{N+1})\right).$$

DOI: 10.1002/fld

Now the time derivative of V can be approximated. In our implementation, we compute

$$\left(\frac{dV}{dt}\right)^{i+1}(T_{N+1}) = \frac{3V^{i+1}(T_{N+1}) - 4V(T_N) + V(T_{N-1})}{2\Delta t_{3D}}. \tag{15}$$

Step 4. Substituting (8) and (9) in (10), we deduce for the pressure on Γ:

$$p_{3D}^{i+1}(T_{N+1}) = (1-\chi)p_{3D}^{i}(T_{N+1}) + \chi\left(\bar{p}^{i+1}(T_{N+1})|_{x=b} - (R_{1D0D} + R_{0D3D})Q_{1D}^{i+1}(T_{N+1}) + R_{0D3D}\left(\frac{dV}{dt}\right)^{i+1}(T_{N+1})\right).$$

Step 5. Solve the linearized 3D Navier–Stokes problem in Ω_{3D} for $\mathbf{u}^{N+1} \approx \mathbf{u}(T_{N+1})$ and $p^{N+1} \approx p(T_{N+1})$:

$$\begin{cases} \frac{3\mathbf{u}^{N+1}-4\mathbf{u}^{N}+\mathbf{u}^{N-1}}{2\Delta t} + (2\mathbf{u}^N - \mathbf{u}^{N-1})\cdot\nabla\mathbf{u}^{N+1} - \nu\Delta\mathbf{u}^{N+1} + \nabla p^{N+1} = \mathbf{f}^{N+1}, \\ \qquad\qquad \operatorname{div}\mathbf{u}^{N+1} = 0, \\ \mathbf{u}^{N+1}|_{\Gamma_0} = 0, \quad \left(-\nu\frac{\partial\mathbf{u}^{N+1}}{\partial\mathbf{n}} + p^{N+1}\mathbf{n}\right)|_{\Gamma_{\text{in}}} = p_{3D}^{i+1}(T_{N+1}), \\ \qquad\qquad \left(-\nu\frac{\partial\mathbf{u}^{N+1}}{\partial\mathbf{n}} + p^{N+1}\mathbf{n}\right)|_{\Gamma_{\text{out}}} = \boldsymbol{\psi}(T_{N+1})\mathbf{n}. \end{cases} \tag{16}$$

Step 6. Finally, calculate the 3D fluid flux:

$$Q_{3D}^{i+1}(T_{N+1}) = \int_{\Gamma} \mathbf{u}^{N+1}\cdot\mathbf{n}\mathbf{d}\mathbf{s}.$$

We note that instead of (10) we enforce in (16) the condition

$$(p_{0D} - p - R_{0D3D}Q_{3D})\mathbf{n} = -\nu\frac{\partial\mathbf{u}}{\partial\mathbf{n}} \quad \text{on } \Gamma,$$

which reduces to (10) only for vanishing viscosity. Although $\nu > 0$ in the model, we use the aforementioned condition, which is somewhat more convenient for a variational formulation of the 3D problem, because it corresponds to the 'do-nothing' condition [11].

3.2. Spatial discretization

For the numerical integration of the 1D model equations, we use the grid-characteristic method [19]. The first order scheme applied to the characteristic form of (2) is conservative, monotone and contains essential dissipative terms for handling non-smooth solutions ([15, 20]). For the 3D model, one has to solve on every time step the linearized Navier–Stokes equations, also known as the Oseen problem:

$$\begin{cases} \beta\mathbf{u} - \nu\Delta\mathbf{u} + (\boldsymbol{w}\cdot\nabla)\,\mathbf{u} + \nabla p = \mathbf{f} \\ \qquad\qquad \operatorname{div}\mathbf{u} = 0, \\ \mathbf{u}|_{\Gamma_0} = \mathbf{0}, \quad \left(\nu\frac{\partial\mathbf{u}}{\partial\mathbf{n}} - p\mathbf{n}\right)|_{\Gamma_{\text{in}}\cup\Gamma_{\text{out}}} = \boldsymbol{\phi} \end{cases} \quad \text{in } \Omega_{3D} \tag{17}$$

where $\mathbf{u} = \mathbf{u}^{N+1}$, $p = p^{N+1}$, $\mathbf{f} = (2\Delta t)^{-1}(4\mathbf{u}^n - \mathbf{u}^{n-1})$, $\mathbf{w} = (2\mathbf{u}^n - \mathbf{u}^{n-1})$, $\beta = 3(2\Delta t)^{-1}$, and the boundary value $\boldsymbol{\phi}$ is defined from the 0D model and outflow condition.

To discretize the Oseen problem (17), we consider a conforming finite element method. We assume a regular subdivision of Ω into tetrahedra. Denote the finite element velocity and pressure spaces by $\mathbb{V}_h \subset H^1(\Omega_{3D})^3$ and $\mathbb{Q}_h \subset L^2(\Omega_{3D})$, respectively. In numerical experiments, we use the

DOI: 10.1002/fld

Taylor-Hood P2-P1 elements. Let $\mathbb{V}_h^0$ be the subspace of $\mathbb{V}_h$ of all FE velocity functions vanishing at $\Gamma_{\text{in}} \cap \Gamma_0$. The discrete problem reads: Find $\mathbf{u}_h \in \mathbb{V}_h$, $\mathbf{u}_h|_{\Gamma_{\text{in}}} = \mathbf{u}_{\text{in}}^h$, and $p_h \in \mathbb{Q}_h$ satisfying

$$\begin{aligned} &\int_\Omega (\beta \mathbf{u}_h \cdot \mathbf{v}_h + \nu \nabla \mathbf{u}_h : \nabla \mathbf{v}_h + (\mathbf{w} \cdot \nabla \mathbf{u}_h) \cdot \mathbf{v}_h - p_h \text{div} \mathbf{v}_h + q_h \text{div} \mathbf{u}_h)\, d\mathbf{x} \\ &= \int_\Omega \boldsymbol{f} \cdot \mathbf{v}_h \, d\mathbf{x} + \int_{\Gamma_{\text{in}} \cup \Gamma_{\text{out}}} \boldsymbol{\phi} \cdot \mathbf{v}_h \, d\mathbf{s} \quad \forall\, \mathbf{v}_h \in \mathbb{V}_h^0,\ q_h \in \mathbb{Q}_h. \end{aligned} \tag{18}$$

The resulting discrete Oseen system is solved by a preconditioned BiCGstab method with relative tolerance in residual of 10^{-6}. For preconditioning, we use the two-parameter threshold ILU factorization from [21]. This linear algebraic problem is solved on every iteration of the domain-decomposition method.

4. NUMERICAL EXPERIMENTS

We start with verifying the formal accuracy of our discretization and the performance of algebraic solvers. For this purpose, we first experiment with a known analytical solution. Further, we run several tests with smooth and discontinuous waveforms posed on the inlet of the 1D model. These tests were suggested in [7] for the purpose of assessing the quality of multiscale coupling conditions. Finally, we study the performance of the geometrical multiscale model for the simulation of a blood flow in a digitally reconstructed right coronary artery.

4.1. Experiment with analytical solution

The purpose of this experiment is to test the performance of the numerical solver for the 1D-0D-3D model in terms of discretization accuracy and iterative methods convergence. Hence, in this experiment, we do not compare the 1D-0D-3D model with the 1D-3D model. For this experiment, we take $\Omega_{3\text{D}} = \{\boldsymbol{x} \in \mathbb{R}^3 \,|\, x \in (-1, 1),\ y^2 + z^2 < 1\}$. The circular cross sections are the inflow and outflow boundaries. Domain $\Omega_{1\text{D}}$ is an interval of length 5; it is coupled to $\Gamma_{\text{in}} = \{\mathbf{x} \in \overline{\Omega}_{3\text{D}} \,|\, x = -1\}$. The analytical solution is given by

$$S = \widehat{S} e^{\alpha(\cos(\beta 2\pi t) - 1)}, \quad u = \alpha e^{-\alpha(\cos(\beta 2\pi t) - 1)} \left(1 - e^{\cos(\beta 2\pi t) - 1}\right), \quad \bar{p} = c_0^2 \alpha \left(\cos(\beta 2\pi t) - 1\right),$$

$$V = \alpha(\cos(\beta 2\pi t) - 1) + \frac{\alpha}{c_0^2}\left(e^{-\cos(\beta 2\pi t)+1} - 1\right), \quad \dot{V} = \beta 2\pi \sin(\beta 2\pi t)\alpha\left(\frac{e^{-\cos(\beta 2\pi t)+1}}{c_0^2} - 1\right),$$

$$\mathbf{u} = \left(\frac{2}{\pi}\left(\widehat{S}\alpha\left(1 - e^{\cos(\beta 2\pi t) - 1}\right) - \beta 2\pi \sin(\beta 2\pi t)\alpha\left(\frac{e^{-\cos(\beta \pi t)+1}}{c_0^2} - 1\right)\right)\left(1 - y^2 - z^2\right), 0, 0\right)^T,$$

$$p = c_0^2 \alpha(\cos(\beta 2\pi t) - 1) - \frac{\beta 2\pi}{\widehat{S}} \alpha \sin(\beta 2\pi t)\alpha e^{-\cos(\beta 2\pi t)+1}\left(\frac{e^{-\cos(\beta 2\pi t)+1}}{c_0^2} - 1\right) + 10(-1-x),$$

with $\alpha = 0.11$ and $\beta = 10$. To match 1D, 0D, and 3D models in this example, we set the model coefficients as follows $R_{1\text{D0D}} = -R_{0\text{D3D}} = -\frac{e^{-\cos(2\pi t)+1}}{\widehat{S}}$ ($R_{1\text{D0D}} < 0$ is not likely to occur in physiologically meaningful models, but here is set negative to obtain analytical solution), $C = \frac{1}{c_0^2}$. The flow problems parameters are $\widehat{S} = \pi$ cm^2, $\rho = 1$ g cm^{-3}, $c_0 = 350$ cm s^{-1}, $\nu = 0.04$ cm^{2}s^{-1}. The solution satisfies all coupling conditions from Section 2.4. The right-hand sides φ, ψ, and $\boldsymbol{f}$ were set accordingly. Thus, we built a synthetic solution to the 1D-0D-3D coupled problem. We shall study the convergence of a discrete solution to this synthetic solution.

The 3D domain was triangulated using the global refinement of an initial mesh. This resulted in the sequence of meshes (further denoted by mesh 1, mesh 2, and mesh 3), with the number of tetrahedra $N_{tet} = 1272, 8403$, and 63,384, respectively. Because we use the first-order scheme for the 1D problem, the mesh size and the time step for the 1D model was divided by 4 at each level

DOI: 10.1002/fld

Table I. Error norms in Ω_{3D} for the test with the analytical solution. Error reduction orders are given in brackets.

	3D		
	Mesh 1	Mesh 2	Mesh 3
$\max_{t\in[0,T]} \|u-u_h\|_{L^2}$	8.00E-002	2.02E-002 (1.98)	4.50E-003 (2.17)
$\left(\int_0^T \|\nabla(u-u_h)\|^2 \mathrm{dt}\right)^{\frac{1}{2}}$	3.90E-001	1.05E-001 (1.89)	2.77E-002 (1.92)
$\left(\int_0^T \|u-u_h\|^2 \mathrm{dt}\right)^{\frac{1}{2}}$	8.10E-002	2.10E-002 (1.94)	5.32E-003 (1.98)
$\left(\int_0^T \|p-p_h\|^2 \mathrm{dt}\right)^{\frac{1}{2}}$	1.11E-003	2.72E-004 (2.03)	6.79E-005 (2.01)
N_{glob}	11.2	14.5	40.5
N_{lin}	8.2	15.4	30.4
χ	0.4	0.4	0.3

Table II. Error norms in Ω_{1D} for the test with the analytical solution.

	1D		
	Mesh 1	Mesh 2	Mesh 3
$\left(\int_0^T \|u-u_h\|^2 \mathrm{dt}\right)^{\frac{1}{2}}$	1.11E-000	2.59E-001 (2.10)	6.66E-002 (1.96)
$\left(\int_0^T \|S-S_h\|^2 \mathrm{dt}\right)^{\frac{1}{2}}$	3.48E-004	7.03E-005 (2.31)	1.86E-005 (1.92)

Error reduction orders are given in brackets.

of 3D refinement, that is, $(\Delta x)_{1D} = 5/16, 5/64, 5/256$ cm and $\Delta t_{1D} = 10^{-5}, 2.5\times10^{-6}, 6.125\times10^{-7}$ s (for all other experiments we use $\Delta t_{1D} = 10^{-5}$). The time step for the 3D model was halved for every level of spacial refinement, so we use $\Delta t_{3D} = 0.008, 0.004, 0.002$ s with mesh 1, mesh 2, mesh 3, respectively. In computations, boundary and initial conditions are taken from the known exact solution. Soft coupling conditions with parameters as previously defined are used on the interface between 1D and 3D.

The natural norms for measuring error in Ω_{3D} are $C((0,T);L^2(\Omega_{3D}))$ and $L^2((0,T);H^1(\Omega_{3D}))$ for velocity and $L^2((0,T);L^2(\Omega_{3D}))$ for pressure. These norms and, additionally, $L^2((0,T);L^2(\Omega_{3D}))$ for velocity error are shown in Table I. Table II shows error norms in Ω_{1D}. Time integrals in the definition of the norms were computed approximately using a quadrature rule, for example, we compute

$$\int_0^T \|\nabla(u-u_h)\|_{L^2}^2 \mathrm{dt} \approx \Delta t \sum_{n=1}^{N} \|\nabla(u(n\Delta t)-u_h^n)\|_{L^2(\Omega_{3D})}^2, \quad N = T(\Delta t)^{-1}.$$

In Table I and further in this section, N_{glob} denotes the average number of domain-decomposition iterations (Section 3.1), and N_{lin} denotes the average number of the preconditioned BiCGstab iterations for the Oseen problem on every outer iteration; χ is the parameter of relaxation. The relaxation parameter ω is equal to 1 in this series of experiments. Values of relaxation parameter χ from the Table I are optimal. They provide the minimal number of the average global iterations. The dependence of the number of global iterations on the choice of the relaxation parameter χ is illustrated in Table III. Because this test intends to verify the formal accuracy of the solver for the case of 1D-0D-3D solver rather than to compare different coupling strategies, we do not show results with hard coupling for this test.

4.2. Sinusoidal pulse wave

In this test, we take Ω_{1D} to model a vessel with radius 1 cm and length 5 cm; likewise, Ω_{3D} is a cylinder with radius 1 cm and length 5 cm; for the elastic sphere, Ω_{0D} the reference cross section

DOI: 10.1002/fld

Table III. Average number of global iterations N_{glob} depending on the relaxation parameter χ for the test with the analytical solution for a sequence of refining meshes.

χ	1.0	0.9	0.8	0.7	0.6	0.5	0.4	0.3	0.2	0.1
Mesh 1	-	-	58.3	26.5	16.7	12.8	11.2	15.4	24.4	48.9
Mesh 2	43.3	41.4	27.5	21.0	17.4	14.9	14.5	21.2	32.7	64.4
Mesh 3	-	-	79.5	72.2	65.4	58.1	48.2	40.5	41.6	76.0

Table IV. Parameters of 0D model depending on the elasticity of 1D vessel.

c_0, cm/s	C, $\mathrm{g^{-1}{\cdot}cm^{4.2}}$	$R_{\mathrm{1D0D}} + R_{\mathrm{0D3D}}$, $\mathrm{g{\cdot}cm^{-4}{\cdot}s^{-1}}$
350	2.5E-6	111.5
700	6.3E-7	223
1050	2.9E-7	334

area and the length, that is, $\widehat{S}$ and l in (14), are taken π cm^2 and 0.1 cm, respectively. A uniform tetrahedral mesh consisting of 19681 elements is build in $\Omega_{3\mathrm{D}}$. A sinusoidal waveform for the flow rate is prescribed at the inlet:

$$Q_{in} = 0.1 \sin\left(\frac{2\pi}{0.3} t\right).$$

Flow parameters are taken to be $\rho = 1\,\mathrm{g}\cdot\mathrm{cm}^{-3}$, $\nu = 0.04\,\mathrm{cm}^2\cdot\mathrm{s}^{-1}$. On the outflow boundary of Ω_{3D}, we set $\gamma = 0$, and the initial condition represents fluid at rest. Numerical solutions are computed with three different values of the 1D model elasticity parameter: $c_0 = 350, 700$, or 1050 cm/s. Parameters of $0D$ model are prescribed following the analysis in Section 2.6, resulting in the values shown in Table IV.

We compare numerical results for the following models:

- 1D-3D flow model: The continuity of the normal stress and fluid flux on the coupling interface is enforced (hard coupling).
- 1D-0D-3D flow model: Coupling parameters as in Table IV (soft coupling).
- 1D flow model: The computational domain is a vessel of 10 cm with non-reflective outflow conditions as defined in [22].

Ideally, one would like to compare all computed results to the full 3D FSI solution. In the absence of this data, we consider a vessel of length 10 cm and non-reflective outflow condition [22]. In this problem, we do not observe backward waves like in case of rigid walls.

Figure 3 shows time plots for the flow rate and cross-section area at the 1D-3D model interface and compares them with the reference graph. From the results, it is clear that the multiscale model with soft coupling provides much more accurate solution with significantly reduced oscillations. As should be expected (assuming that the 3D model replaces a compliant vessel with same elasticity properties as modeled by the 1D system), increasing the stiffness of the 1D model leads to the better matching of the 1D-0D-3D model solutions and the referent solution.

From numerical experiments, it occurs that the accuracy of the soft coupling is most dependent on a suitable choice of the total resistance $R_{\mathrm{total}} = R_{\mathrm{1D0D}} + R_{\mathrm{0D3D}}$. Experimenting with various distribution of R_{total} between R_{1D0D} and R_{0D3D} demonstrated less than 1% difference in the results for flow rate and p_{3D} on the interface. Hence, further, we set $R_{\mathrm{0D3D}} = 0$ and vary R_{1D0D}. To illustrate this and to assess the optimality of the choice based on (13), we experimented with different values of the total resistance and monitor the error between the computed solutions and the reference solution. Thus, Figure 4 shows the L^2 norm of the error in the cross-section area and the flow rate at the interface. It is remarkable that the choice of the total resistance given by (13) is (almost) optimal with respect to both error indicators. The conclusion appears to be true for all $c_0 \in \{350\mathrm{cm/s},\ 700\mathrm{cm/s},\ 1050\mathrm{cm/s}\}$.

DOI: 10.1002/fld

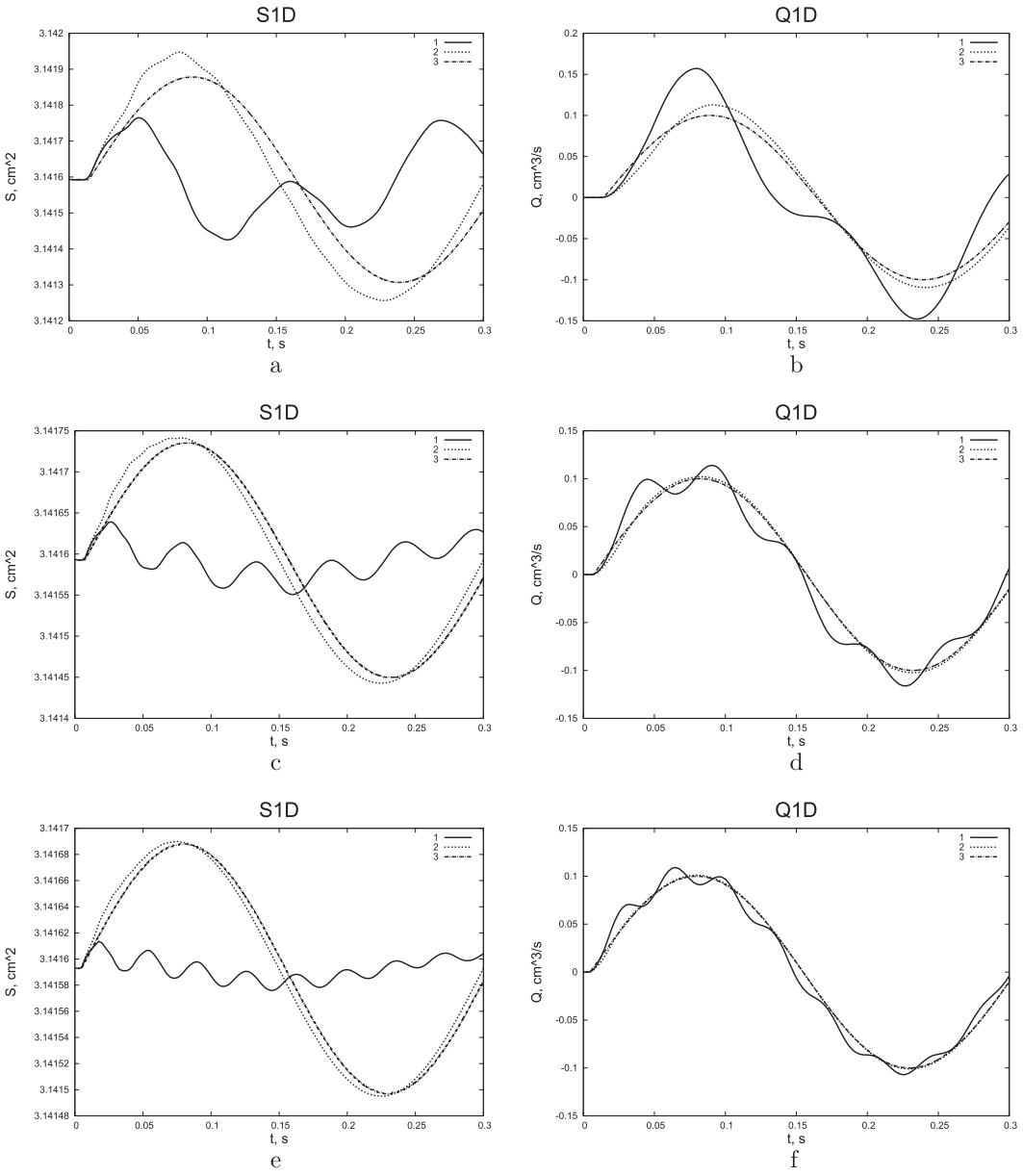

Figure 3. Time plots of the cross-section area and flow rate at $x = b$ computed with different models: (1) 1D-3D (hard coupling), (2) 1D-0D-3D (soft coupling), and (3) reference. Results are shown for several 1D elasticity parameters: Plots (a) and (b) are for $c_0 = 350$ cm/s; plots (c) and (d) are for $c_0 = 700$ cm/s; and plots (e) and (f) are for $c_0 = 1050$ cm/s.

4.3. Step pulse wave

We perform a series of experiments using the same flow models and parameters as above, but with a difference inflow waveform:

$$Q_{in} = \begin{cases} 0.1 \text{ for } t \leqslant 0.1, \\ 0 \text{ for } t > 0.1. \end{cases} \tag{19}$$

Figure 5 shows time plots for the flow rate at the 1D-3D model interface and compares them with the reference graph. Similar to the previous series of experiments with smooth waveform, the results show that the multiscale model with soft coupling provides a much more accurate solution.

DOI: 10.1002/fld

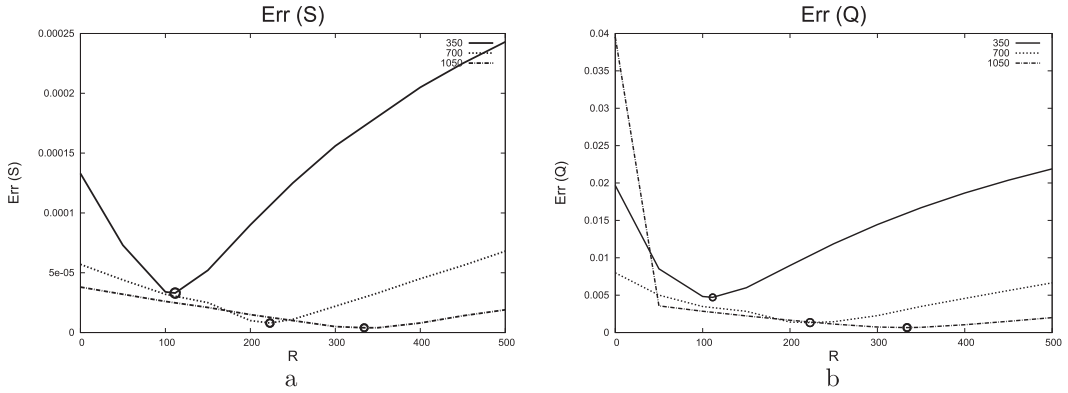

Figure 4. Error L^2 norms for (a) cross-section area (S) in cm^2 and (b) flow rate (Q) in $\mathrm{cm}^3 \cdot \mathrm{s}^{-1}$ depending on the choice of R_{1D0D} (measured in $\mathrm{g{\cdot}cm^{-4}{\cdot}s^{-1}}$) in the 1D-0D-3D model for $c_0 = 350, 700, 1050$ cm/s. Circles mark results obtained with the choice of R_{1D0D} according to (13).

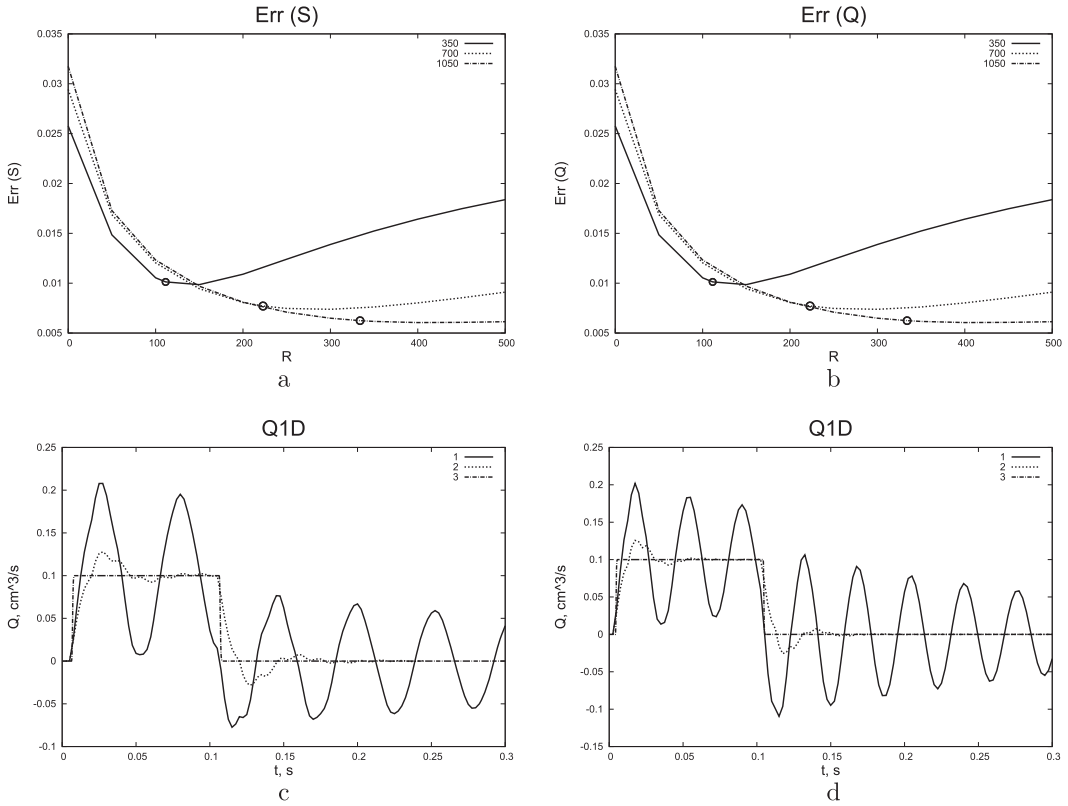

Figure 5. Step pulse wave experiment: Two upper figures show error L^2 norms for (a) cross-section area (S) in cm^2 and (b) flow rate (Q) in $\mathrm{cm}^3 \cdot \mathrm{s}^{-1}$ depending on the choice of R_{1D0D} (measured in $\mathrm{g{\cdot}cm^{-4}{\cdot}s^{-1}}$) in the 1D-0D-3D model for $c_0 = 350, 700, 1050$ cm/s. Circles mark results obtained with the choice of R_{1D0D} according to (13). Figure 3(c)–(d) show time evolution of the flow rate at $x = b$ computed with different models: (1) 1D-3D (hard coupling), (2) 1D-0D-3D (soft coupling), and (3) reference. Results are shown for several 1D elasticity parameters: Plot (c) is for $c_0 = 700$ cm/s, and plot (d) is for $c_0 = 1050$ cm/s.

Handling the discontinuity of the incoming wave is challenging for coupling conditions. Although oscillations are present in the 1D-0D-3D model numerical solution, the solution captures the larger scale pattern, while the hard coupling results in the lost of this principle information. Again, the choice of the total resistance given by (13) is close to optimal with respect to error in both flow rate and cross-section area for all $c_0 \in \{350\,cm/s,\ 700\,cm/s,\ 1050\,cm/s\}$.

DOI: 10.1002/fld

Further, we experiment with the same inflow waveform, but different values of the expansibility parameter C in the 0D model. The choice of the first relaxation parameter $\omega = 1$ does not lead to convergent iteration for larger values of C. Table V shows the number of average global iterations depending on the values of C and ω with fixed $\chi = 0.4$. The '-' sign indicates no convergence.

Additionally, we couple to the downstream part of the 3D domain a simple 1D domain representing a single vessel of length 5 cm. For downstream coupling, we used boundary conditions (4)–(5)

Table V. Average number of global iteration depending on the relaxation parameter ω for C increased 10 or 100 times, and $c = 350, 700, 1050$ cm/s.

	10			100		
ω	C = 2.5E-5 c = 350 cm/s	C = 6.3E-6 c = 700 cm/s	C = 2.9E-6 c = 1050 cm/s	C = 2.5E-4 c = 350 cm/s	C = 6.3E-5 c = 700 cm/s	C = 2.9E-5 c = 1050 cm/s
0.9	-	-	34.7	-	-	-
0.7	-	20.2	14.4	-	-	-
0.5	27.1	17.3	13.4	-	-	-
0.3	20.9	16.0	17.6	-	-	-
0.1	28.7	33.3	29.9	-	23.2	22.6
0.09				-	23.4	23.2
0.07				29.3	24.3	23.2
0.05				23.9	25.5	24.1
0.03				25.9	30.2	37.6
0.01				48.3	84.04	98.0

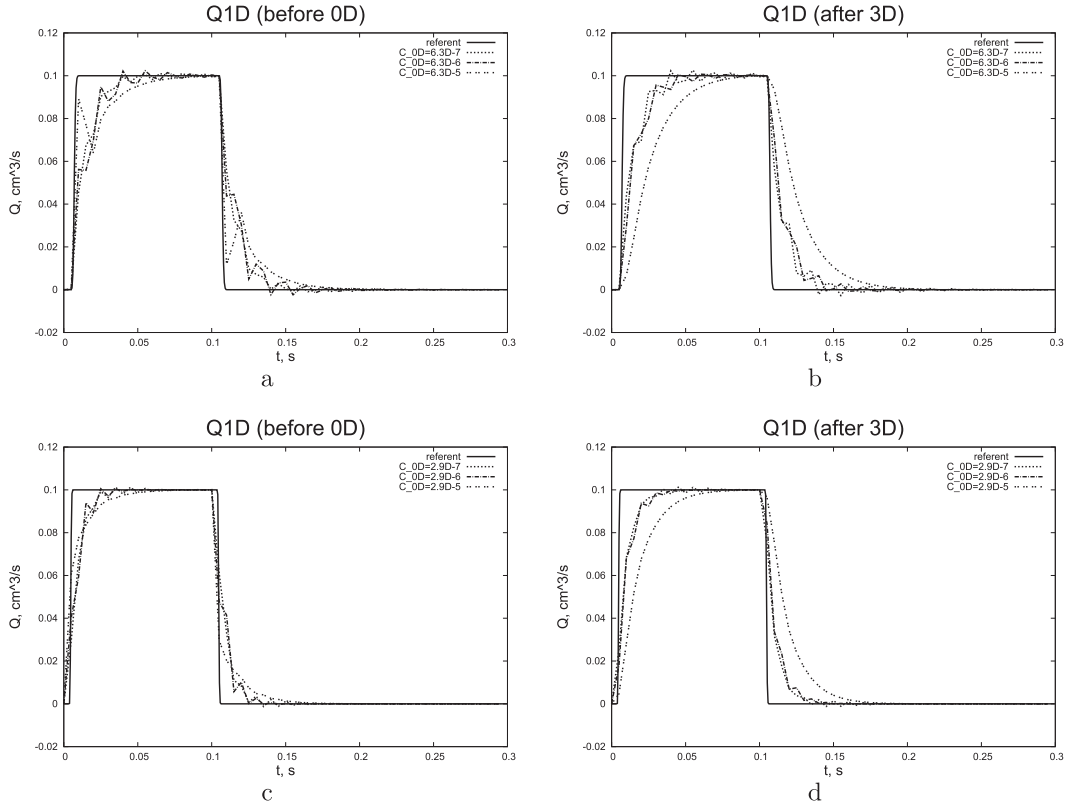

Figure 6. Time evolution of the flow rate in the step pulse wave experiment with $c_0 = 700$ cm/s in Figure 6(a)–(b) and $c_0 = 1050$ cm/s in Figure 6(c)–(d). Figure 6(a) and (c) show the 1D flow rate before 0D model on the upstream 3D boundary, while Figures 6(b) and (d) show the flow rate at the downstream 3D boundary. Each figure shows graphs of the flow rate computed for different values of the elasticity parameter C in the 0D model.

DOI: 10.1002/fld

and the splitting numerical algorithm described in [9]. The effect of choosing larger expansibility parameters is illustrated in Figure 6. The plots in Figure 6 show the 1D flow rates before 0D model and at the downstream 3D boundary. The increasing of C by a factor of 10 compared with the one given by (14) with $l = 0.1$ leads to quite similar results, while the values large by a factor of 100 significantly smear the computed solution and increase the time shift compared to the reference profile.

4.4. Flow in a right coronary artery

Finally, we study the performance of the new geometrical multiscale model for the simulation of a blood flow in a right coronary artery. The 3D part of the artery is treated as rigid; so in this model example, the variation of exterior pressure due to the cardiac muscle contraction is ignored. The geometry of the 3D flow domain was recovered from a real patient coronary CT angiography. The ANI3D package [23] was used to generate the tetrahedral mesh (Figure 7). The diameter of the inlet cross-section is about 0.27 cm, and the whole domain can be embedded in a parallelogram with sides 6.5 cm × 6.8 cm × 5 cm. The mesh consists of 120,191 tetrahedra leading to the discrete system for the 3D flow problem with 623 883 of unknowns. Other 3D model parameters are $\nu = 0.04\,\mathrm{cm}^2/\mathrm{s}$, $\rho = 1\,\mathrm{g/cm}$. The 1D domain $\Omega_{1\mathrm{D}}$ represents a single vessel with length 1 cm and diameter 0.27 cm. The speed of small disturbance propagation in the wall of a coronary artery was found 1,312 cm/s [24]. This defines the elasticity c_0 parameter in our 1D model. The inlet velocity waveform is shown in Figure 8; it was suggested in [25] on the basis of clinical measurements (see also [26]). This waveform is used to define the flow rate at the left boundary of the 1D model. The Neumann boundary condition $-\nu(\nabla\mathbf{u})\cdot\mathbf{n} + p\mathbf{n} = \mathbf{0}$ was imposed on all outflow boundaries of the 3D domain. One cardiac cycle period was 0.735 s.

Parameters of the 0D model were computed from (13), (14) as follows: $C = 3.5\cdot 10^{-9}$ $\mathrm{cm}^4\cdot\mathrm{s}^2\cdot\mathrm{g}^{-1}$ (length of vessel represented by 0D model is assumed to be 0.13 cm, equal to radius of the 1D vessel), $R_{1\mathrm{D}0\mathrm{D}} + R_{0\mathrm{D}3\mathrm{D}} = 17894\ \mathrm{g}\cdot\mathrm{s}^{-1}\cdot\mathrm{cm}^{-4}$. For the linear solver, we used the preconditioned BiCGstab method and the two-parameter ILU(τ_1, τ_2) preconditioner, with $\tau_1 = 0.03$, $\tau_2 = 7\tau_1^2$ (see [21] for more details); $\chi = 0.5$ was taken in the domain–decomposition iterations. The time step in the 1D model was equal to 10^{-5} s and in the 3D model $(\Delta t)_{3D} = 2.5\cdot 10^{-3}$ s. This results in the average numbers of 10 outer and 150 inner iterations per 3D time step.

The results of computations are shown in Figures 8 and 9. When the 1D-0D-3D multiscale model is used, both the flow rate and the vessel cross-section area on the interface follow the waveform prescribed on the inlet with minor oscillations. For the hard 1D-3D coupling, the oscillations on the 1D-3D interface are somewhat more pronounced. For this experiment we do not have a reference solution. Velocity and pressure fields computed in the 3D part of the model both look reasonable (Figure 9).

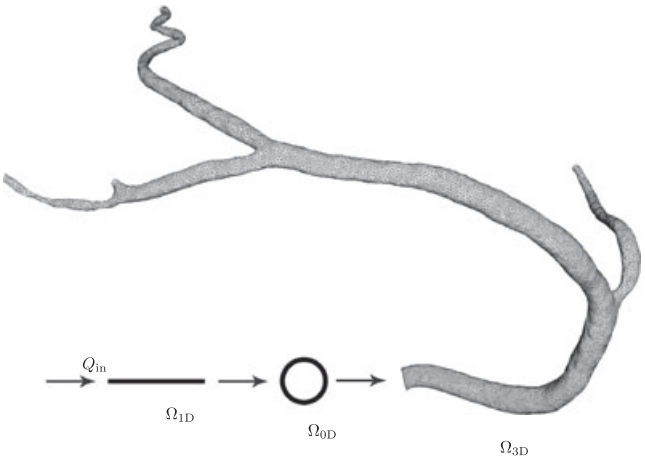

Figure 7. Multiscale 1D-0D-3D model of the right coronary artery.

DOI: 10.1002/fld

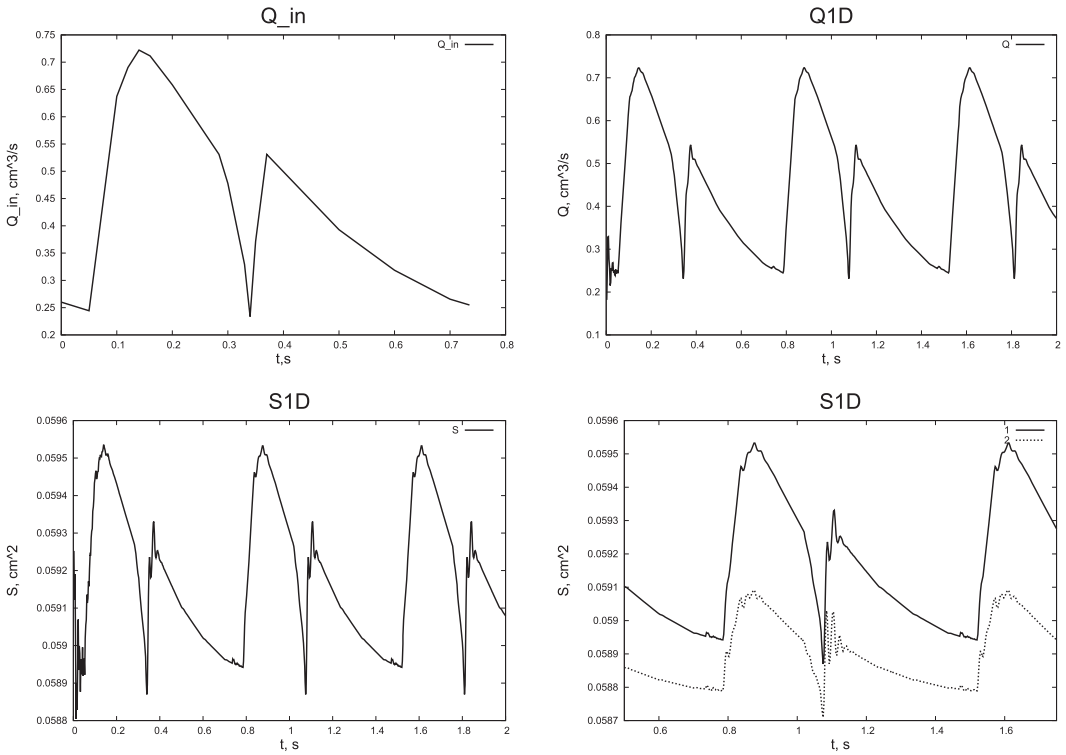

Figure 8. Upper-left: the velocity (flow rate) waveform on the inflow of Ω_{1D}. Upper-right: flow rate computed on the interface (with soft coupling) over few cycles. Bottom-left: vessel cross-section area computed on the interface (with soft coupling) over few cycles. Bottom-right: the difference in computed cross-section areas with soft (solid line) versus hard (dotted line) couplings.

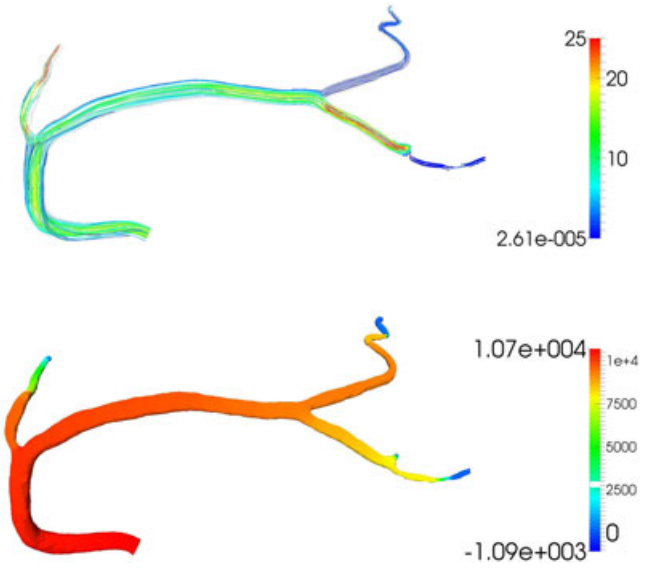

Figure 9. Top picture shows selected steamlines colored by the velocity absolute value (cm/s) at time 1.6 s; Bottom picture shows the pressure distribution (g cm^{-1} s^{-2}) at time 1.6 s

5. CONCLUSIONS

To suppress numerical oscillations resulting from coupling 1D compliant and 3D rigid blood flow models, we introduce a 0D model on the 1D-3D interface. This auxiliary system of ODEs models

DOI: 10.1002/fld

the kinematics of an elastic sphere under small deformations. The studies show that the model acts as an absorbing device and, to a certain extent, mimics the missing compliance of the 3D model. The system of ODEs depends on several parameters. The paper demonstrated that these parameters can be chosen based on simple mechanical principles, and the choice appears to be close to optimal. Numerical experiments show that for a smooth waveform the multiscale model is able to preserve the flow rate and cross-section area at the interface with a high level of accuracy. For the waveform with discontinuity, oscillations are not removed completely, but the principle information is correctly preserved. We use a domain-decomposition approach to iterate between subproblems for the coupled solution. The convergence of the iterations was found sensitive to the value of the parameter C in the 0D problem. Further research is required to search for a more robust iterative algorithm. At the same time, a Krylov subspace method with a special ILU type preconditioner was very efficient to solve linearized 3D flow problem in such geometries like a reconstructed right coronary artery. Treating walls of the 3D model rigid is crucial for gaining this 3D solver efficiency.

ACKNOWLEDGEMENTS

The results of T. Dobroserdova presented in Sections 2.4, 2.5, 3.1, and 4.1 were supported by the Russian Federation President Grant for Young Scientists, MK-6121.2015.1. Joint author results presented in the other sections were supported by the Russian Science Foundation, Grant No. 14-31-00024. The authors are grateful to the staff of I.M. Sechenov First Moscow State Medical University and especially to Ph. Kopylov, N. Gagarina, E. Fominykh, and A. Dzyundzya for providing patient-specific data.

REFERENCES

1. Formaggia L, Gerbeau JF, Nobile F, Quarteroni A. On the coupling of 3D and 1D Navier–Stokes equations for flow problems in compliant vessels. *Computer Methods in Applied Mechanics and Engineering* 2001; **191**(6-7):561 –582. Minisymposium on Methods for Flow Simulation and Modeling.
2. Lagana K, Balossino R, Migliavacca F, Pennati G, Bove EL, de Leval MR, Dubini G. Multiscale modeling of the cardiovascular system: application to the study of pulmonary and coronary perfusions in the univentricular circulation. *Journal of Biomechanics* 2005; **38**(5):1129 –1141.
3. Formaggia L, Nobile F, Quarteroni A, Veneziani A. Multiscale modelling of the circulatory system: a preliminary analysis. *Computing and Visualization in Science* 1999; **2**(2-3):75–83.
4. Oshima M, Torii R, Tokuda S, Yamada S, Koizumi A. Patient-specific modeling and multi-scale blood simulation for computational hemodynamic study on the human cerebrovascular system. *Current Pharmaceutical Biotechnology* 2012; **13**(11):2153–65.
5. Urquiza S, Blanco P, Venere M, Feijoo R. Multidimensional modelling for the carotid artery blood flow. *Computer Methods in Applied Mechanics and Engineering* 2006; **195**(33-36):4002–4017.
6. Nachit A, Panasenko G, Abdelmalek Z. Asymptotic partial domain decomposition in thin tube structures: numerical experiments. *Journal for Multiscale Computational Engineering* 2013; **11**(5):407–441.
7. Passerini T, de Luca M, Formaggia L, Quarteroni A, Veneziani A. A 3D/1D geometrical multiscale model of cerebral vasculature. *Journal of Engineering Mathematics* 2009; **64**(4):319–330.
8. Hillen B, Hoogstraten HW, Post L. A mathematical model of the flow in the circle of willis. *Journal of Biomechanics* 1986; **19**(3):187–194.
9. Dobroserdova TK, Olshanskii MA. A finite element solver and energy stable coupling for 3D and 1D fluid models. *Computer Methods in Applied Mechanics and Engineering* 2013; **259**:166–176.
10. Formaggia L, Moura A, Nobile F. On the stability of the coupling of 3D and 1D fluid-structure interaction models for blood flow simulation. *Mathematical Modelling and Numerical Analysis* 2007; **41**(4):743–769.
11. Heywood JG, Rannacher R, Turek S. Artificial boundaries and flux and pressure conditions for the incompressible Navier–Stokes equations. *International Journal for Numerical Methods in Fluids* 1996; **22**:325–352.
12. Euler L. Principia pro motu sanguinis per arterias determinando. *Opera Posthuma Mathematica et Physica Anno* 1844; **2**:814–823.
13. Abakumov M, Gavrilyuk K, Esikova N, Lukshin A, Mukhin S, Sosnin N, Tishkin V, Favorskij A. Mathematical model of the hemodynamics of the cardio-vascular system. *Differential Equations* 1997; **33**(7):895–900.
14. Formaggia L, Quarteroni A, Veneziani A. *Cardiovascular Mathematics: Modeling and Simulation of the Circulatory System*, Vol. 1. Springer, MS&A: Milano, 2009.
15. Simakov S, Kholodov A. Computational study of oxygen concentration in human blood under low frequency disturbances. *Mathematical Models and Computer Simulations* 2009; **1**(2):283–295.

DOI: 10.1002/fld

16. Blanco PJ, Watanabe SM, Passos MARF, Lemos P, Feijoo RA, An anatomically detailed arterial network model for one-dimensional computational hemodynamics. *IEEE Transactions on Biomedical Engineering* 2015; **62**(2): 736–753.
17. Malossi A, Blanco P, Crosetto P, Deparis S, Quarteroni A. Implicit coupling of one-dimensional and three-dimensional blood flow models with compliant vessels. *Multiscale Modeling & Simulation* 2013; **11**(2): 474–506.
18. Alastruey J, Moore S, Parker K, David T, Peiró J, Sherwin S. Reduced modelling of blood flow in the cerebral circulation: coupling 1-D, 0-D and cerebral auto-regulation models. *International Journal for Numerical Methods in Fluids* 2008; **56**(8):1061–1067.
19. Magomedov KM, Kholodov AS. *Net-Characteristic Numerical Methods*. Nauka, Moscow: Moscow, 1988.
20. Vassilevskii Y, Simakov S, Salamatova V, Ivanov Y, Dobroserdova T. Numerical issues of modelling blood flow in networks of vessels with pathologies. *Russian Journal of Numerical Analysis and Mathematical Modelling* 2011; **26**(6):605–622.
21. Konshin IN, Olshanskii MA, Vassilevski YV. ILU preconditioners for non-symmetric saddle point matrices with application to the incompressible Navier–Stokes equations. *SIAM Journal on Scientific Computing* 2015; **37**(4):A2171–A2197.
22. Lin BW, Lu PJ. High-resolution Roe's scheme and characteristic boundary conditions for solving complex wave reflection phenomena in a tree-like arterial structure. *Journal of Computational Physics* 2014; **260**:143–162.
23. Lipnikov K, Vassilevski Y. Advanced numerical instruments 3D. Avialable from: http://sourceforge.net/projects/ani3d.
24. Aguado-Sierra J, Parker K, Davies J, Francis D, Hughes A, Mayet J. Arterial pulse wave velocity in coronary arteries. *Proceedings of the 28th IEEE EMBS Annual International Conference*, New York City, 2006; 867–870.
25. Jung J, Hassanein A, Lyczkowski R. Hemodynamic computation using multiphase flow dynamics in a right coronary artery. *Annals of Biomedical Engeneering* 2006; **34**(3):393–407.
26. Levy MN. *Principles of physiology*. Elsevier Mosby: St. Louis, 2000.

DOI: 10.1002/fld